

Ultra-Luminous X-Ray Sources in the Most Metal Poor Galaxies

A.H. Prestwich

Harvard-Smithsonian Center for Astrophysics, 60 Garden Street, Cambridge, MA 02138

Maria Tsantaki

University of Crete, Physics Department, 71003 Heraklion, Crete, Greece & Centro de Astrofisica, Universidade do Porto, Rua das Estrelas, 4150-762 Porto, Portugal

A. Zezas

Harvard-Smithsonian Center for Astrophysics, 60 Garden Street, Cambridge, MA 02138 & University of Crete, Physics Department, 71003 Heraklion, Crete, Greece & Foundation for Research and Technology-Hellas, 71110 Heraklion, Crete, Greece

F. Jackson

Harvard-Smithsonian Center for Astrophysics, 60 Garden Street, Cambridge, MA 02138

T.P. Roberts

Department of Physics, University of Durham, South Road, Durham DH1 3LE, UK

R. Foltz

Department of Physics and Astronomy, University of California, Riverside, 900 University Avenue, Riverside, CA 92521

T. Linden

University of Santa Cruz, Department of Physics 211 Interdisciplinary Sciences Building, 1156 High Street, Santa Cruz, CA 95064, USA

V. Kalogera

Center for Interdisciplinary Exploration and Research in Astrophysics (CIERA) & Department of Physics and Astronomy, Northwestern University, 2145 Sheridan Road, Evanston, IL 60208, USA

ABSTRACT

Ultra-Luminous X-ray sources (ULX) are X-ray binaries with $L_x > 10^{39}$ ergs s^{-1} . The most spectacular examples of ULX occur in starburst galaxies and are now understood to be young, luminous High Mass X-ray Binaries. The conditions under which ULX form are poorly understood, but recent evidence suggests they may be more common in low metallicity systems. Here we investigate the hypothesis that ULX form preferentially in low metallicity galaxies by searching for ULX in a sample of Extremely Metal Poor Galaxies (XMPG) observed with the *Chandra* X-ray Observatory (CXO). XMPG are defined as galaxies with $\log(O/H) + 12 < 7.65$, or less than 5% solar. These are the most metal-deficient galaxies known, and a logical place to find ULX if they favor metal poor systems. We compare the number of ULX (corrected for background contamination) per unit of star formation ($N_{ULX}(SFR)$) in the XMPG sample with $N_{ULX}(SFR)$ in a comparison sample of galaxies with higher metallicities taken from the Spitzer Infrared Galaxy Sample (SINGS). We find that ULX occur preferentially in the metal poor sample with a formal statistical significance of 2.3σ . We do not see strong evidence for a trend in the formation of ULX in the high metallicity sample: above $12 + \log(O/H) \sim 8.0$ the efficiency of ULX production appears to be flat. The effect we see is strongest in the lowest metallicity bin. We discuss briefly the implications of these results for the formation of black holes in low metallicity gas.

1. Introduction

Ultra-Luminous X-ray sources (ULX) are X-ray binaries with $L_x > 10^{39}$ ergs s^{-1} most commonly found in star forming and starburst galaxies. These sources have attracted considerable attention in recent years because they have broad-band X-ray luminosities many times the Eddington limit for a neutron star or stellar mass black hole (Miller & Colbert 2004; Roberts 2007; Feng & Soria 2011). Some of these extreme objects may be intermediate mass black holes ($M > 500 M_\odot$, (Colbert & Mushotzky 1999; Farrell et al. 2009; Sutton et al. 2012)). It seems likely, however that most ULX are stellar X-ray sources which are either radiating in excess of the Eddington limit and/or have black-hole masses somewhat higher than is commonly seen in black hole candidates in Milky Way binaries ($M > 10 M_\odot$, Roberts (2007); Gladstone et al. (2009); Zampieri & Roberts (2009)). ULX are found in a wide variety of systems – spirals, interacting starbursts and dwarf galaxies. However, the conditions under which ULX form are poorly understood.

It is well established that the number of ULX in star forming galaxies scales with the

star formation rate (Grimm et al. 2003; Ranalli, Comastri, & Setti 2003; Mapelli et al. 2010; Mineo et al. 2012). In addition, there are several lines of evidence to suggest that ULX form preferentially in low metallicity gas. Kaaret, Schmitt, & Gorski (2011) found that the ratio of X-ray luminosity to star formation rate is an order of magnitude larger in low metallicity Blue Compact Dwarf Galaxies than for solar metallicity star forming galaxies. Swartz et al. (2008) found that the occurrence rate per unit galaxy mass is higher in dwarfs than in more massive galaxies (see also Walton et al. (2011)). This surprising correlation is explained if ULX favor the metal poor environments found in dwarfs. Evidence that there is a direct connection between metallicity and ULX production was presented by Mapelli et al. (2010) who find an anti-correlation between the number of ULX and metallicity based on a sample of 64 galaxies. A further study by Mapelli et al. (2011) with the addition of two XMPG came to the same conclusion. Spectroscopy of ULX counterparts and surrounding gas also suggest that ULX are formed from stars in metal poor gas (e.g. Soria et al. (2005); Liu et al. (2007)).

Here we investigate the hypothesis that ULX form preferentially in low metallicity galaxies by searching for ULX in a sample of Extremely Metal Poor Galaxies (XMPG) observed with the *Chandra* X-ray Observatory (*CXO*). XMPG are defined as galaxies with $\log(O/H) + 12 < 7.65$, or less than 5% solar (Papaderos et al. 2008). These are the most metal-deficient galaxies known, and a logical place to find ULX if they favor metal poor systems. Our goal is to compare the number of ULX (normalized to the star formation rate and accounting for cosmic background sources) in a sample of XMPG with a comparison sample of galaxies with higher metallicities taken from the Spitzer Infrared Galaxy Sample (SINGS). For a sample of galaxies we define $N_{ULX}(SFR)$ to be:

$$N_{ULX}(SFR) = \frac{\sum N_{ULX} - \sum N_{BKG}}{\sum SFR} \quad (1)$$

Here $\sum N_{ULX}$ is the total number of ULX found in a sample of galaxies (e.g. the XMPG sample), $\sum N_{BKG}$ the total number of expected cosmic background sources (with an apparent luminosity $> 10^{39}$ ergs s^{-1}) in the same sample and $\sum SFR$ is the integrated star formation rate (in M_{\odot} per year) of the sample galaxies.

2. Galaxy sample

Our sample is listed in Table 1. It consists of 25 nearby ($d \leq 50$ Mpc) extremely metal poor galaxies ($(O/H) + 12 < 7.65$). These are the most metal-deficient galaxies known. Most of those are Blue Compact Dwarf galaxies. Three galaxies in the sample (I Zw18, SBS

0335-052, SBS 0335-052W) were observed with Chandra in 2000 (Thuan et al. 2004). The remainder were observed as part of a Cycle 11 Large Project. The exposure times were set to obtain a 3.5σ detection of a point source of luminosity 7.8×10^{38} ergs cm $^{-2}$ s $^{-1}$ (i.e. our survey is complete down to 7.8×10^{38} ergs cm $^{-2}$ s $^{-1}$.) Completeness is further discussed in Section 3.1. Observational details are given in Table 2.

3. X-Ray Observations

All observations were obtained with the back-illuminated chip ACIS-S3 except for the galaxies SBS 0335-052 and SBS 0335-052W, which were observed with the front-illuminated ACIS-I3 camera. The observations were performed in VFAINT mode. We reprocessed raw data (level 1 event files) using Chandra Interactive Analysis of Observations software (CIAO), version 4.2 and the CALibration DataBase (CALDB), version 4.3.0. Standard routines were used to correct for bad pixels, charge transfer inefficiency and time dependent gain. A new Level 2 events file was created by filtering for standard grades (0, 2, 3, 4, 6) and rejecting grades associated with bad pixels.

The positions of X-ray sources were determined with the CIAO tool WAVDETECT. This tool is a wavelet-based source detection algorithm (Freeman et al. 2002). The X-ray image is convolved with a wavelet function to produce a "correlation image". Clumps of counts (sources) are identified as a local maximum in the correlation image if the scale of the wavelet is approximately equal to (or greater than) the size of the clump. Hence, WAVDETECT also gives an estimate of the size of the source. It is typically run with wavelets of differing scales to better detect extended emission.

WAVDETECT was run on the level 2 files in the 0.3-8keV band using scales of 1.0, 2.0, 4.0, 8.0 and 16.0 pixels. We set a threshold significance for identifying a pixel as belonging to the source at 10^{-6} . All the detected sources have scales consistent with their being point sources. Sources within the D₂₅ region (defined as the elliptical contour best corresponding to the 25 mag arcsec $^{-2}$ blue isophote de Vaucouleurs et al. (1991)) were considered to be associated with the galaxy. The results of the source detection are shown in Table 3.

Source regions were defined based on the WAVDETECT source extent. We also create the corresponding background regions by setting apertures with larger radii than the sources. We perform photometry for these sources, using the `dmextract` tool. The results of the photometry are shown at Table 5. The source counts per pixel follow the Poisson distribution and the count error, since the number of counts is very low, the Gehrels approximation: error = $1 + \sqrt{(N + 0.75)}$ (Gehrels 1986).

Table 1: The Extremely Metal Poor Galaxy sample.

Galaxy	R.A. (J2000)	Dec. (J2000)	Distance (Mpc)	D ₂₅ (arcmin)	N _H (10 ²⁰ cm ⁻²)	12+log(O/H)
UGC 772	08h25m55.5s	+35d32m32s	3.10	1.20×0.90	11.5	7.24±0.03
SDSS J210455.31-003522.2	21h04m55.3s	-00d35m22s	13.7	-	6.47	7.26±0.03
SBS 1129+576	11h32m02.5s	+57d22m46s	26.3	0.75×0.10	0.87	7.41±0.07
HS 0822+3542	08d25m55.5s	+35d32m32s	12.7	0.27×0.12	4.82	7.35
SDSS J120122.32+021108.5	12h01m22.3s	+02d11m08s	18.4	0.35×0.12	1.88	7.55±0.03
RC2 A1116+51	11h19m34.3s	+51d30m12s	20.8	0.24×0.17	1.19	7.51±0.04
SBS 0940+544	09h44m16.6s	+54d11m34s	24.7	1.22×1.54	1.34	7.48
KUG 1013+381	10h16m24.5s	+37d54m46s	19.6	0.38×0.25	1.41	7.58
SBS 1415+437	14h17m01.4s	+43d30m05s	10.4	0.75×0.15	1.21	7.60
6dF J0405204-364859	04h05m20.3s	-36d49m01s	11.0	0.48×0.35	0.88	7.34
SDSS J141454.13-020822.9	14h14m54.1s	-02d08m23s	24.6	0.34×0.24	4.17	7.32
SDSS J223036.79-000636.9	22h30m36.8s	-00d06m37s	18.0	0.24×0.20	5.20	7.64
UGCA 292	12h38m40.0s	+32d46m01s	3.5	1.00×0.70	1.34	7.27±0.08
HS 1442+4250	14h44m12.8s	+42d37m44s	10.5	1.13×0.26	1.53	7.63
KUG 0201-103	02h04m25.6s	-10d09m35s	22.7	0.46×0.19	2.08	7.56
SDSS J081239.52+483645.3	08h12m39.5s	+48d36m45s	9.04	0.46×0.23	4.58	7.16
SDSS J085946.92+392305.6	08h59m46.9s	+39d23m06s	10.9	0.39×0.27	2.44	7.45
KUG 0743+513	07h47m32.1s	+51d11m28s	8.6	0.70×0.30	5.17	7.68
KUG 0937+298	09h40m12.8s	+29d35m30s	11.2	0.62×0.23	1.87	7.45
KUG 0942+551	09h46m22.8s	+54d52m08s	24.4	0.37×0.18	1.23	7.66
SBS 1102+606	11h05m53.7s	+60d22m29s	19.9	0.60×0.28	0.59	7.64±0.04
RC2 A1228+12	12h30m48.5s	+12d02m42s	21.2	0.29×0.16	2.47	7.64
I Zw 18	09h34m02.0s	+55d14m28s	17.1	0.30×0.20	1.99	7.17
SBS 0335-052	03h37m44.0s	-05d02m40s	52.6	0.23×0.20	4.98	7.25±0.05
SBS 0335-052W	03h37m38.4×s	-05d02m37s	52.2	0.10×0.13	4.96	7.10±0.08

NOTES: Distances are taken from the NASA/IPAC Extragalactic Database (NED). D₂₅ shows the diameter of major×minor axis. The Galactic N_H is calculated with Colden tool, <http://cxc.harvard.edu/toolkit/colden.jsp>. Metallicities are taken from literature. For the galaxy SDSS J210455.31-003522.2 we used the optical diameter from NASA/SAO Image Archive.

Table 2: X-ray observations

Galaxy	Obs.ID	Date	Exposure (sec)	Instrument
UGC 772	11281	30-08-2009	5081	ACIS-S3
SDSS J210455.31-003522.2	11282	04-09-2009	5007	ACIS-S3
SBS 1129+576	11283	06-07-2010	14755	ACIS-S3
HS 0822+3542	11284	20-12-2009	51200	ACIS-S3
SDSS J120122.32+021108.5	11286	23-11-2009	8097	ACIS-S3
RC2 A1116+51	11287	07-11-2009	11640	ACIS-S3
SBS 0940+544	11288	18-01-2010	16828	ACIS-S3
KUG 1013+381	11289	24-01-2010	9402	ACIS-S3
SBS 1415+437	11291	30-10-2009	5114	ACIS-S3
6dF J0405204-364859	11292	28-05-2010	5010	ACIS-S3
SDSS J141454.13-020822.9	11293	18-12-2009	16680	ACIS-S3
SDSS J223036.79-000636.9	11294	25-09-2009	7715	ACIS-S3
UGCA 292	11295	06-11-2009	5007	ACIS-S3
HS 1442+4250	11296	26-11-2009	5188	ACIS-S3
KUG 0201-103	11297	06-09-2009	13590	ACIS-S3
SDSS J081239.52+483645.3	11298	18-12-2009	4777	ACIS-S3
SDSS J085946.92+392305.6	11299	18-12-2009	4782	ACIS-S3
KUG 0743+513	11300	18-12-2009	5073	ACIS-S3
KUG 0937+298	11301	16-01-2010	5007	ACIS-S3
KUG 0942+551	11302	19-01-2010	16020	ACIS-S3
SBS 1102+606	11285	23-08-2010	10340	ACIS-S3
RC2 A1228+12	11290	26-07-2010	12200	ACIS-S3
I Zw 18	805	08-02-2000	40750	ACIS-S3
SBS 0335-052	796	07-09-2000	59742	ACIS-I3
SBS 0335-052W	796	07-09-2000	59742	ACIS-I3

The flux of an X-ray source is proportional to the net count rate, where the constant of proportionality depends on the response of the detector and the assumed source spectrum:

$$A = \frac{Flux}{CountRate}, [(erg/sec/cm^2)/(counts/sec)] \quad (2)$$

We extracted standard spectral responses (the Redistribution Matrix (RMF) and Area Response Matrix) and simulated a spectrum for each source. Using the results of Swartz et al. (2004), we adopt an intrinsic source spectrum with photon index $\Gamma=1.7$ and assume values

Table 3: X-ray source detection.

Galaxy	Number of sources	Position	
		R.A. (J2000)	Dec. (J2000)
SBS 1129+576	1	11h32m02.57s	+57d22m36.87s
RC2 A1116+51	1	11h19m34.13s	+51d30m12.48s
SBS 0940+544	1	09h44m16.44s	+54d11m34.39s
I ZW 18	1	09h34m01.97s	+55d14m28.23s
SBS 0335-052	1	03h37m44.04s	-05d02m39.89s
SBS 0335-052W	1	03h37m38.44s	-05d02m37.14s

for galactic absorption taken from Dickey & Lockman (1990) . We then estimate the constant A from the ratio of the number of counts to the calculated flux in the simulated spectrum. Fluxes and luminosities were constructed in the 0.3-8 keV band, using the constant A derived from the simulated spectra. They are shown in Table 5. One source, IZw18, had enough counts to perform a spectral fit. The best fit is consistent with the analysis of Thuan et al. (2004) and is shown in Table 4. The fluxes and luminosities of the other sources are shown in Table 5

Table 4: Spectral fit to I ZW 18.

Galaxy	Source count-rate (counts/sec)	Γ	N_H (10^{20} cm^{-2})	χ^2/dof
I ZW 18	0.0111	$1.88^{+0.22}_{-0.20}$	$7.54^{+4.76}_{-6.17}$	12.69/19

Table 5: X-ray Photometry

Galaxy	Net counts	Background counts	N_H ($10^{20} F \text{ cm}^{-2}$)	Flux ($10^{-15} \text{ erg/cm}^2/\text{sec}$)	L_x (10^{39} erg/sec)
SBS 1129+576	21.47±5.71	0.19±1.97	0.87	1.14±0.3	0.72±0.19
RC2 A1116+51	89.04±10.48	0.21±1.98	1.19	5.95±0.70	2.93±0.35
SBS 0940+544	39.20±7.32	0.20±1.97	1.34	1.81±0.34	1.26±0.24
I ZW 18	494.44±23.25	1.56±2.51	7.54	7.46±0.35	4.92±0.25
SBS 0335-052	28.21±6.38	1.30±2.43	4.98	0.56±0.13	1.86±0.42
SBS 0335-052W	116.29±11.82	1.30±2.43	4.96	2.31±0.23	7.53±0.77

3.1. Completeness and Background Sources

In this section we demonstrate that our sample of ULX in the metal-poor galaxies is complete: i.e. that we are not "missing" ULX due to inadequate exposure. In addition, we estimate the number of ULX which are chance coincidences: background AGN that happen to align with the optical galaxy.

The completeness limit is expressed by the source detection probability of a galaxy . It is a function of the source and background intensity, measured in counts. The detection probability as a function of source counts and background counts/pixel can be parameterized by the following function (Zezas et al. 2007):

$$A(C) = 1.0 - \lambda_0 C^{-\lambda_1} e^{-\lambda_2 C} \quad (3)$$

where C is the source intensity in counts, λ_0 , λ_1 , λ_2 parameters that depend on the background counts per pixel.

All galaxies of our sample were measured to have background level below 0.025 counts per pixel. The best-fit parameters for this background give a detection probability of the form:

$$A(C) = 1.0 - 11.12 C^{-0.83} e^{-0.43 C}. \quad (4)$$

Therefore, by solving the equation for 90% and 50% completeness, the corresponding source counts are: $C_{90} = 7.2$ counts and $C_{50} = 4.4$ counts.

Table 6 shows that all luminosities of 90% completeness and all luminosities 50% completeness, are well under the limit of 10^{39} ergs s⁻¹ cm². This means that we have detected at least 90% of all existing ULX sources in the galaxy sample.

The predicted number of background sources for each galaxy was estimated as follows. For each galaxy, we calculate the 0.3-8 keV flux for a source of 10^{39} ergs s⁻¹ and then transform the flux to the 0.5-2 keV band assuming a power law source spectrum with photon index $\Gamma=1.7$ and a foreground N_H listed in Table 1. We then used the LogN-LogS curves of Giacconi et al. (2001) for the 0.5-2 KeV band to estimate the number of background sources per square degree and normalize by the D_{25} values to get the absolute number of background sources predicted to lie within the optical area of the galaxy. These values are given in Table 6. We note that SBS 0940+544 has a predicted background value close to one.

Table 6: Completeness

Galaxy	Exposure time (sec)	90% (10^{38} erg/sec)	50% (10^{38} erg/sec)	N_{BKG}
UGC 772	5081	1.66	1.01	0.014
SDSS J210455.31-003522.2	5007	2.39	1.46	0.039
SBS 1129+576	14755	2.40	1.47	0.034
HS 0822+3542	5120	2.00	1.23	0.004
SDSS J120122.32+021108.5	8097	2.66	1.63	0.010
RC2 A1116+51	11640	2.37	1.45	0.012
SBS 0940+544	16828	2.31	1.41	0.776
KUG 1013+381	9402	2.60	1.59	0.026
SBS 1415+437	5114	1.35	0.82	0.010
6dF J0405204-364859	5010	1.54	0.94	0.017
SDSS J141454.13-020822.9	16680	2.31	1.41	0.034
SDSS J223036.79-000636.9	7715	2.67	1.63	0.012
UGCA 292	5007	0.08	0.05	0.041
HS 1442+4250	5188	1.35	0.83	0.028
KUG 0201-103	13590	2.41	1.47	0.031
SDSS J081239.52+483645.3	4777	1.09	0.67	0.008
SDSS J085946.92+392305.6	4782	1.58	0.97	0.011
KUG 0743+513	5073	0.93	0.57	0.014
KUG 0937+298	5007	1.59	0.97	0.015
KUG 0942+551	16020	2.36	1.45	0.027
SBS 1102+606	10340	2.44	1.49	0.048
RC2 A1228+12	12200	2.37	1.43	0.014
I ZW 18	25956	0.72	0.44	0.013
SBS 0335-052	59742	4.74	2.89	0.070
SBS 0335-052W	59742	4.66	2.85	0.020

4. Estimates of the Star Formation Rate in the XMPG Sample

It is well established that the number of ULX in a galaxy scales with the star formation rate (Grimm et al. 2003; Ranalli, Comastri, & Setti 2003; Mapelli et al. 2010; Mineo et al. 2012). We therefore need reliable estimates of the star formation rate in the XMPG sample in order to determine whether $N_{ULX}(SFR)$ is higher in the metal poor sample than in the SINGS sample. We use two methods to estimate the star formation rate: the Far Ultraviolet (FUV) luminosity from *GALEX* and the $24\mu\text{m}$ luminosity from *Spitzer*.

4.1. GALEX Data

The FUV emission from star forming regions comes directly from young massive O and B stars. We use the method from Hunter et al. (2010) to relate the FUV luminosity to the star formation rate in dwarf galaxies:

$$SFR_{\text{FUV}}(M_{\odot}/\text{yr}) = 1.27 \times 10^{-28} L_{\text{FUV}}(\text{ergs}^{-1}\text{Hz}^{-1}) \quad (5)$$

We obtained GALEX FUV images from the GalexView version 1.4.6 catalog. All galaxies in the XMPG sample were detected with the exception of SDSS J223036.79-000636.9. This galaxy is excluded from the rest of the analysis in this paper. Source counts were extracted using the *CIAO* DMEXTRACT routine. This was done with either circular or elliptical source apertures, depending on the morphology of the galaxy in question, as well as an annular background aperture. Both of these apertures were centered on the source, with the circular apertures having a radius of either 10 or 15 pixels, and the ellipses having a semi-major and semi-minor axis of length 28 and 14 pixels or 15 and 7.5 pixels, respectively, depending on the size of the source. All background annuli had an area 8 times that of their respective source apertures. The fluxes were computed using the relationship $f_{\text{FUV}} = (1.4 \times 10^{-15}) \times \text{count rate}^1$. Note that these fluxes are in units of $\text{erg cm}^{-2} \text{s}^{-1} \text{\AA}^{-1}$. We converted these values to units of $\text{erg cm}^{-2} \text{s}^{-1} \text{Hz}^{-1}$ by multiplying them by λ^2/c , where λ is the effective wavelength of the FUV detector ($= 1528 \text{\AA}$), and c is the speed of light in units of \AA s^{-1} . With the fluxes in these new units, we proceeded to calculate the L_{FUV} values of the sources, which were subsequently corrected for extinction. We then calculated the SFR_{FUV} estimates of the galaxies using the extinction-corrected luminosities.

¹http://galexgi.gsfc.nasa.gov/docs/galex/FAQ/counts_background.html

Table 7: UV measurements and SFRs

Galaxy	E(B-V) ⁽¹⁾	Count Rate ⁽²⁾	L_{FUV} ⁽³⁾	SFR _{FUV} ⁽⁴⁾
	(mag)	(ct s ⁻¹)	($\times 10^{26}$ erg s ⁻¹ Hz ⁻¹)	($10^{-3} M_{\odot}$ yr ⁻¹)
UGC 772	0.028	5.55 \pm 0.05	0.09 \pm 0.001	1.09 \pm 0.01
SDSS J210455.31-003522.2	0.066	1.21 \pm 0.06	0.49 \pm 0.02	6.22 \pm 0.29
SBS 1129+576	0.013	3.48 \pm 0.20	3.47 \pm 0.20	44.02 \pm 2.52
HS 0822+3542	0.047	1.08 \pm 0.09	0.32 \pm 0.03	4.11 \pm 0.33
SDSS J120122.32+021108.5	0.024	1.20 \pm 0.03	0.64 \pm 0.02	8.07 \pm 0.20
RC2 A1116+51	0.015	4.38 \pm 0.21	2.58 \pm 0.12	32.76 \pm 1.57
SBS 0940+544	0.013	1.56 \pm 0.11	1.37 \pm 0.10	17.41 \pm 1.25
KUG 1013+381	0.015	7.63 \pm 0.26	4.24 \pm 0.15	53.87 \pm 1.87
SBS 1415+437	0.009	12.69 \pm 0.30	1.93 \pm 0.05	24.55 \pm 0.59
6dF J0405204-364859	0.006	5.29 \pm 0.22	0.80 \pm 0.03	10.12 \pm 0.43
SDSS J141454.13-020822.9	0.058	0.63 \pm 0.02	0.78 \pm 0.02	9.88 \pm 0.30
UGCA 292	0.016	7.15 \pm 0.18	0.13 \pm 0.003	1.62 \pm 0.04
HS 1442+4250	0.013	9.00 \pm 0.22	1.42 \pm 0.04	18.08 \pm 0.45
KUG 0201-103	0.021	1.30 \pm 0.09	1.02 \pm 0.07	13.00 \pm 0.87
SDSS J081239.52+483645.3	0.051	0.86 \pm 0.02	0.13 \pm 0.003	1.71 \pm 0.04
SDSS J085946.92+392305.6	0.026	0.71 \pm 0.01	0.14 \pm 0.001	1.72 \pm 0.02
KUG 0743+513	0.070	12.58 \pm 0.34	1.66 \pm 0.04	21.12 \pm 0.57
KUG 0937+298	0.018	5.21 \pm 0.16	0.97 \pm 0.03	12.34 \pm 0.37
KUG 0942+551	0.012	1.48 \pm 0.12	1.26 \pm 0.10	16.01 \pm 1.27
SBS 1102+606	0.006	4.19 \pm 0.17	2.27 \pm 0.09	28.79 \pm 1.14
RC2 A1228+12	0.027	2.69 \pm 0.04	2.03 \pm 0.03	25.69 \pm 0.39
I ZW18	0.032	11.52 \pm 0.08	5.60 \pm 0.04	71.12 \pm 0.52
SBS 0335-052	0.047	5.52 \pm 0.20	28.41 \pm 1.00	360.86 \pm 12.76
SBS 0335-052W	0.046	0.56 \pm 0.01	2.84 \pm 0.04	36.07 \pm 0.53

Notes: ⁽¹⁾ Reddening magnitude of the source, used to calculate source extinction; ⁽²⁾

Observed background-subtracted source count rate; ⁽³⁾ Extinction-corrected far-UV luminosity of the source; ⁽⁴⁾ Star-formation rate, calculated using the formula from Hunter et al. (2010).

4.2. Spitzer Data

The $24\mu\text{m}$ emission in galaxies comes from single photon transient heating of small grains and can be used as a tracer of recent star formation. Calzetti et al. (2007) derived the following relation between the star formation rate (SFR) and $24\mu\text{m}$ emission from calibrating H_{II} regions in nearby galaxies:

$$SFR_{\text{IR}}(M_{\odot}/\text{yr}) = 1.31 \times 10^{-38} [L_{24\mu\text{m}}(\text{ergs}/\text{sec})]^{0.885}, \quad (6)$$

where for intermediate luminosity galaxies:

$$1 \times 10^{40} < L_{24\mu\text{m}} < 3 \times 10^{44} \text{ erg/sec}$$

We acquired data from the Spitzer space telescope that were obtained with the MIPS instrument in the 24 microns band. We obtained the post-BCD (post Basic Calibrated Data) data for the 9 galaxies in the sample that have available MIPS $24\mu\text{m}$ data. The data sets consist of several exposures that are interpolated into one mosaic image. From these images we measure the surface brightness in units of MJy/sr. The post-BCD product mosaic pixel sizes are $2.42 \times 2.45 \text{ arcsec}^2$ for the 24 microns detector.

We perform aperture photometry using funtools. We define an aperture for the source with an ellipse that includes the total flux of the source and an elliptical annulus for the background region as depicted in Figures 15 - 16 for the 9 galaxies. In order to calculate the total flux density of each source, we sum the total flux of the source, subtract the background, on a set of pixels and multiply by the number of steradian per pixel. We convert the surface brightness to the flux density with the following formula:

$$f_v = \sum_{\text{pixels}} 2.45 \times 2.45 \frac{\text{arc sec}^2}{\text{pixel}} \times 0.023504 \frac{\text{Flux}}{\text{arc sec}^2} [\text{mJy}]. \quad (7)$$

The flux density is converted to monochromatic flux:

$$F = \frac{c}{\lambda} f_v(\lambda). \quad (8)$$

The uncertainty on the flux is calculated from the mosaic variance image by adding in quadrature the uncertainty of all pixels within the source aperture. The results are listed at Table 8.

4.3. Comparison of *Spitzer* and *GALEX* star formation rates

Several galaxies in the XMPG sample have both *GALEX* UV images and *Spitzer* 24 μm data. It is therefore instructive to compare SFR derived from the two methods. Figure 1 shows the star formation rate derived from the FUV flux with the star formation rate derived from the 24 μm flux. There is a clear correlation between the two methods. The rate derived from the FUV flux is systematically higher than for the 24 μm flux. This is almost certainly because 24 μm emission underestimates the star formation rate because of the very low dust content of the XMPG. We adopt the *GALEX* derived star formation rate because (1) the *Spitzer* 24 μm data likely underestimates the star formation rate, and (2) it is available for all the galaxies. We note that SBS 0335-052 appears to have very high SFR in comparison with the other XMPGs.

5. The SINGS sample.

In order to determine whether there is a statistically significant excess of ULX in the most metal poor systems, we require a comparison sample of galaxies with well determined star formation rates and metallicities. The *Spitzer* Infrared Nearby Galaxies Survey (Kennicutt et al. 2003) is ideal for this purpose. It is a comprehensive imaging and spectroscopic study of 75 nearby galaxies with distances < 30 Mpc. The morphological types of the sample range from elliptical to irregular. The SINGS sample does not include absolute extremes in properties that can be found in larger volumes such as ULIRGs, luminous AGNs or extremely metal poor galaxies. A distance-limited sample of the SINGS survey has been observed by *Chandra* (Jenkins et al in preparation). We use a sub-sample of SINGS galaxies selected by Calzetti et al. (2007) which have Hubble Space Telescope (HST) NICMOS images in the Pa α hydrogen emission line (1.8756 μm), H α observations and *Chandra* observations. The H α and the Pa α lines are used to measure the extinction correction. Furthermore, the Pa α line is used to calibrate the mid-infrared emission. There are 33 galaxies in the Calzetti et al. (2007) sample, 26 of which also form part of the *Chandra* survey. The galaxies are divided into three groups according to their oxygen abundance: High-metallicity galaxies [$12+\log(\text{O}/\text{H}) \geq 8.35$], Intermediate-metallicity galaxies [$8.00 < 12+\log(\text{O}/\text{H}) \leq 8.35$], and Low-metallicity galaxies [$12+\log(\text{O}/\text{H}) \leq 8.00$]. For reference, the XMPGs have metallicities $12+\log(\text{O}/\text{H}) \leq 7.65$. We list the main characteristics of the SINGS sample in Table 9.

The metallicities given in Table 9 are given as an upper and lower bound and taken from Moustakas et al. (2010). The lower bound is the metallicity derived using the calibration of Pilyugin & Thuan (2005) (hereafter PT05) and the upper bound using the calibration of Kobulnicky & Kewley (2004) (hereafter KK04). As discussed in Moustakas et al. (2010), the

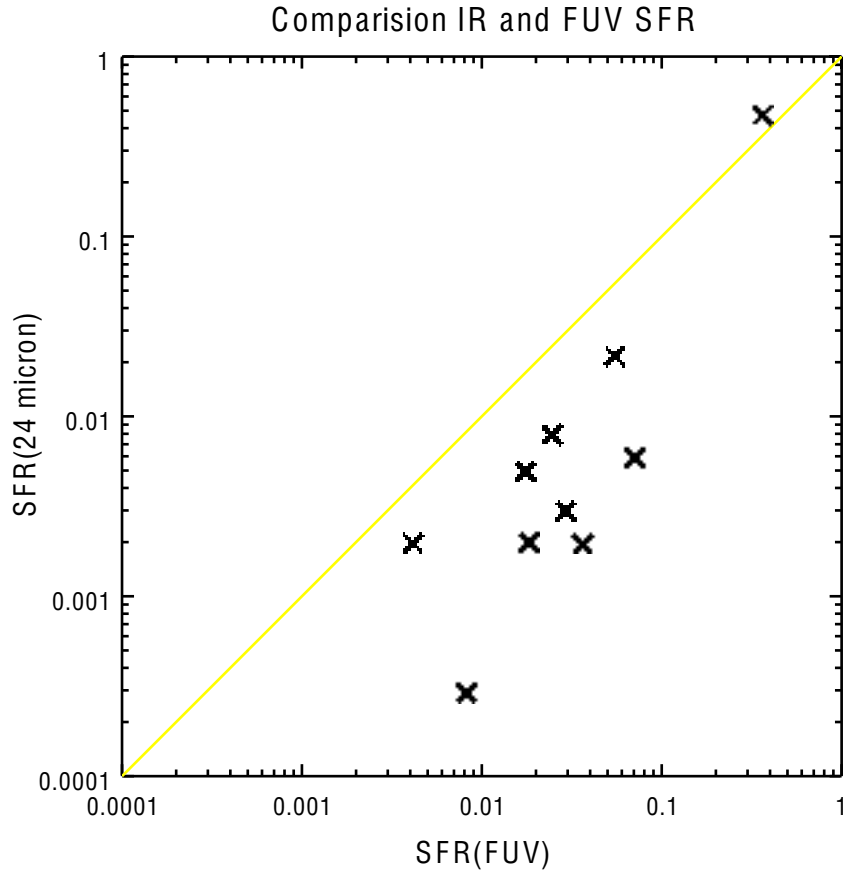


Fig. 1.— Comparison of the star formation rate determined from the FUV luminosity and 24- μ m luminosity. The line denotes $\text{SFR}_{IR} = \text{SFR}_{FUV}$.

PT05 calibration is based on empirical abundance measurements of individual HII regions and the KK04 calibration on photoionization model calculations. The KK04 calibration gives abundances that are systematically higher than PT05. In this paper we choose the PT05 calibration since this method was used to derive the XMPG abundances. The results of this paper are unchanged if we use KK04 or an average of the two.

We estimate the star formation rate of the SINGS galaxies using the calibration of Calzetti et al. (2010):

$$SFR(M_{\odot}/yr) = 5.5 \cdot 10^{-42} \times [L(H\alpha)_{obs} + 0.02L(24\mu m)] \quad (9)$$

Note that the $L(H\alpha)_{obs}$ is the observed $H\alpha$ luminosity without correction for internal dust attenuation.

We use the measurements of the $H\alpha$ and $24\mu m$ fluxes of Dale et al. (2007)) and Kennicutt et al. (2008) & Kennicutt et al. (2009). The numbers of ULX for the SINGS sample have been provided by *Chandra* SINGS team (Jenkins et al in preparation).

6. Comparison between the SINGS and XMPGs samples

In this section, we investigate the relationship between metallicity and $N_{ULX}(SFR)$. Table 10 compares $N_{ULX}(SFR)$ for the XMPG sample and the SINGS sample. The SINGS sample is divided into 3 sub-groups according to metallicity values (High, Intermediate and Low metallicity). In addition, we show $N_{ULX}(SFR)$ obtained by combining the SINGS low metallicity sample and the XMPG sample. The difference in $N_{ULX}(SFR)$ between the high metallicity SINGS galaxies and the low metallicity galaxies (comprising the XMPG and low metallicity SINGS galaxies) is 2.3σ . The low metallicity sample has a small number of individual galaxies with very high N_{ULX}/SFR values (these have low SFR and one ULX). A Kolmogorov-Smirnov (K-S) test gives the probability that the two distributions (low metallicity and SINGS) come from the same parent population as 0.18. Finally, Figure 2 shows $N_{ULX}(SFR)$ as a function of metallicity. The high metallicity SINGS galaxies are plotted as individual points, and the XMPG and SINGS low metallicity galaxies are combined. We note that for galaxies with no ULX, the background-subtracted number of ULX is negative, which is unphysical. There is a marked increase in $N_{ULX}(SFR)$ in the low metallicity galaxies. We conclude that ULX form preferentially in low metal systems, with the caveat that the formal significance of this result is low.

We do not find any evidence for a trend in $N_{ULX}(SFR)$ with metallicity $12+\log(O/H)>8.0$.

Fitting the data points in Figure 2 above $12+\log(\text{O}/\text{H})=8.0$ with both a flat line (slope 0) and a straight line with non-zero slope we find that the more complex model (non-zero slope) is slightly preferred on the basis of a χ^2 fit. We use an F-test to determine whether the model with a slope is significantly better than the flat line (the null hypothesis is that a slope does not give a statistically better fit). The F-test gives a significance of 0.35, confirming that a slope is not required.

Mapelli et al. (2010) use a larger sample of galaxies and find an anti-correlation between $N_{ULX}(SFR)$ and metallicity (their Figure 5 is directly comparable to Figure 2 of this paper). As discussed in the previous paragraph, there may be a similar trend in the SINGS galaxies but the effect is small below $12+\log(\text{O}/\text{H})=8.0$ and the scatter is large. We cannot unambiguously confirm this result. The preference for ULX to form at the low metallicities is most apparent in the lowest metallicity bin.

6.1. Summary and Discussion

In this paper, we present the results of a Chandra survey to search for ULX in the most metal poor galaxies. We find that, compared to a comparison sample of high metallicity SINGS galaxies, the low metallicity galaxies are more likely to host a ULX. The number of ULX normalized to the star formation rate is ~ 0.17 for the high metallicity galaxies and 7.0 for the low metallicity systems ($12+\log(\text{O}/\text{H})<8.0$). The formal significance of this result is low. This study broadly agrees with the results of Mapelli et al. (2011) who also find that the number of ULX increases in lower metallicity galaxies. Mapelli et al. (2011) also claim to see a trend in the numbers of ULX as a function of metallicity. As demonstrated in Figure 2, we do not see strong evidence that $N_{ULX}(SFR)$ decreases as a function of metallicity above ~ 8.0 . This result suggests there maybe a "threshold" for more efficient ULX formation at about $12+\log(\text{O}/\text{H})<8$.

In a recent paper, we (Prestwich et al. 2012) compared the ULX population of two collisional ring galaxies, the Cartwheel and NGC 922. The Cartwheel has a relatively low metallicity ($12+\log(\text{O}/\text{H})\sim 8.1$) and NGC 922 has a metallicity close to solar ($12+\log(\text{O}/\text{H})\sim 8.81$). We found that the number of ULXs in NGC 922 and the Cartwheel scales with the star formation rate: we do not find any evidence for an excess of sources in the Cartwheel relative to NGC 922. The $N_{ULX}(SFR)$ values for NGC 922 and the Cartwheel are the same (within the errors) as the SINGS galaxies. This is demonstrated in Figure 3 where we plot $N_{ULX}(SFR)$ vs. metallicity for the SINGS galaxies, the Cartwheel and NGC 922. The KK04 calibration is used for this plot as it is more appropriate for the Cartwheel and NGC 922 measurements. Figure 3 adds to the evidence that the high number of ULX in the Cartwheel is due to it's

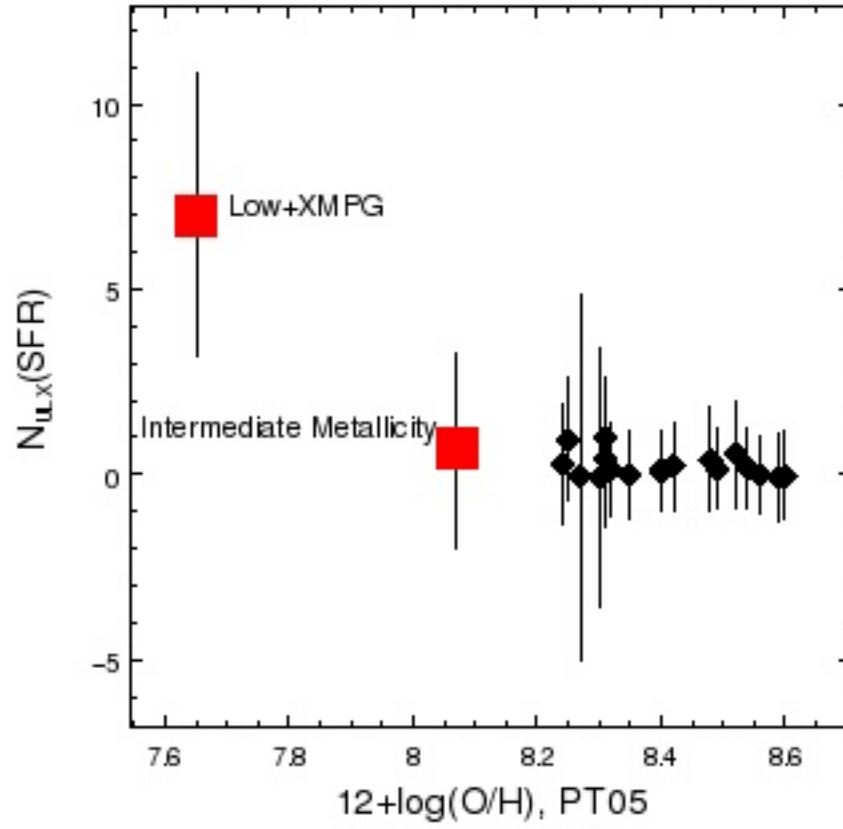


Fig. 2.— $N_{ULX}(SFR)$ for individual SINGS galaxies, intermediate metallicity galaxies and the combined metal poor and XMPG. This plot uses the PT05 metallicity calibration.

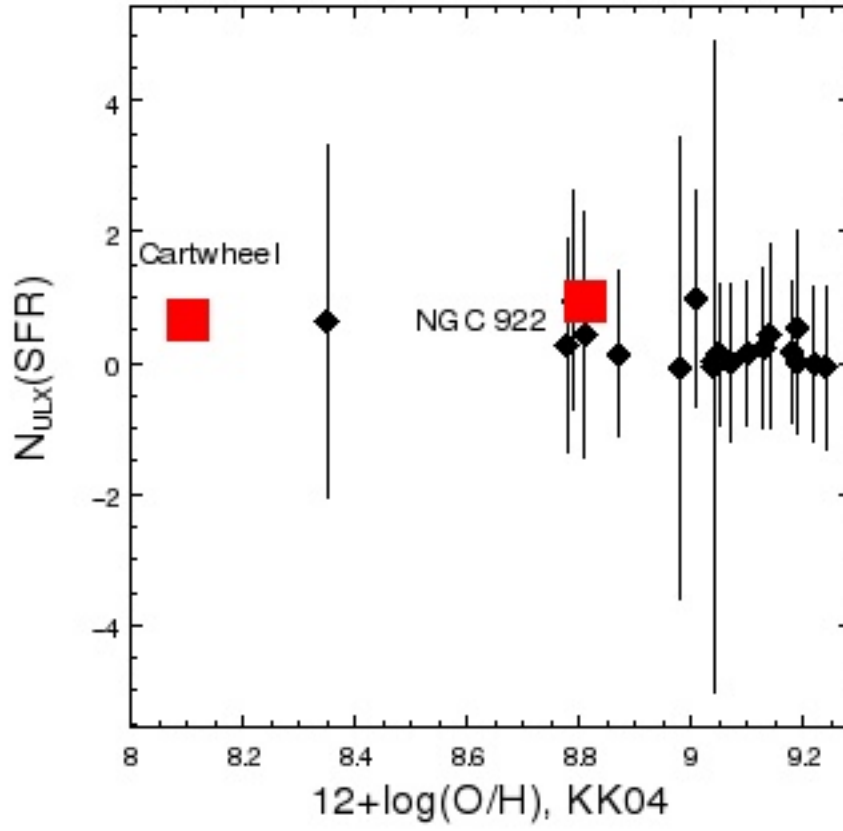


Fig. 3.— $N_{ULX}(SFR)$ for individual SINGS galaxies, NGC 922 and the Cartwheel. This plot uses the KK04 metallicity calibration.

very high star formation rate, and not a metallicity effect.

There are two hypotheses which might explain the excess of ULX in metal-poor galaxies. Linden et al. (2010) studied the effect of metallicity on HMXB production and found that the number of ULX in low metal systems increased dramatically below a threshold of $Z/Z_{\odot} < 10\%$. The high X-ray luminosities derive from Roche Lobe Overflow onto a black hole, which typically has a mass $M \leq 10M_{\odot}$. The threshold predicted by Linden et al. (2010) is consistent with the increase in $N_{ULX}(SFR)$ we see in galaxies with $12+\log(O/H) < 8$. An alternate hypothesis is that higher mass black holes are able to form in lower metallicity gas (Mapelli et al. 2009; Zampieri & Roberts 2009) leading to higher X-ray luminosities in HMXB. Our results are consistent with both of these scenarios.

7. Acknowledgements

Thanks to the Leigh Jenkins and the *Chandra* SINGS teams for providing results prior to publication, to Doug Swartz for giving us details of galaxies with no detected ULX and to the referee Michela Mapelli for helping to clarify many points in the paper. Support for this work was provided by the National Aeronautics and Space Administration through Chandra Award Number G0-11108A issued by the Chandra X-ray Observatory Center, which is operated by the Smithsonian Astrophysical Observatory for and on behalf of the National Aeronautics Space Administration under contract NAS8-03060. This research has made use of the NASA/IPAC Extragalactic Database (NED) which is operated by the Jet Propulsion Laboratory, California Institute of Technology, under contract with the National Aeronautics and Space Administration. Based on observations made with the NASA Galaxy Evolution Explorer. GALEX is operated for NASA by the California Institute of Technology under NASA contract NAS5-98034

REFERENCES

- Calzetti, D., et al. 2007, ApJ, 666, 870
- Calzetti, D., et al. 2010, ApJ, 714, 1256
- Colbert, E. J. M., & Mushotzky, R. F. 1999, ApJ, 519, 89
- Dale, D. A., et al. 2007, ApJ, 655, 863
- de Vaucouleurs, G., de Vaucouleurs, A., Corwin, H. G., Jr., Buta, R. J., Paturel, G., &

- Fouque, P. 1991, Volume 1-3, XII, 2069 pp. 7 figs.. Springer-Verlag Berlin Heidelberg New York,
- Dickey, J. M., & Lockman, F. J. 1990, ARA&A, 28, 215
- Farrell, S. A., Webb, N. A., Barret, D., Godet, O., & Rodrigues, J. M. 2009, Nature, 460, 73
- Feng, H., & Soria, R. 2011, New A Rev., 55, 166
- Freeman, P. E., Kashyap, V., Rosner, R., & Lamb, D. Q. 2002, ApJS, 138, 185
- Gehrels, N. 1986, ApJ, 303, 336
- Giacconi, R., et al. 2001, ApJ, 551, 624
- Grimm, H.-J., Gilfanov, M., & Sunyaev, R. 2003, MNRAS, 339, 793
- Gilfanov, M., Grimm, H.-J., & Sunyaev, R. 2004, MNRAS, 347, L57
- Gladstone, J. C., Roberts, T. P., & Done, C. 2009, MNRAS, 397, 1836
- Goad, M. R., Roberts, T. P., Reeves, J. N., & Uttley, P. 2006, MNRAS, 365, 191
- Hunter, D. A., Elmegreen, B. G., & Ludka, B. C. 2010, AJ, 139, 447
- Kaaret, P., Schmitt, J., & Gorski, M. 2011, ApJ, 741, 10
- Kennicutt, R. C., Jr., et al. 2003, PASP, 115, 928
- Kennicutt, R. C., Jr., et al. 2009, ApJ, 703, 1672
- Kennicutt, R. C., Jr., Lee, J. C., Funes, S. J., José G., Sakai, S., & Akiyama, S. 2008, ApJS, 178, 247
- Kobulnicky, H. A., & Kewley, L. J. 2004, ApJ, 617, 240
- Linden, T., Kalogera, V., Sepinsky, J. F., Prestwich, A., Zezas, A., & Gallagher, J. S. 2010, ApJ, 725, 1984
- Liu, J.-F., Bregman, J., Miller, J., & Kaaret, P. 2007, ApJ, 661, 165
- Liu, J.-F., & Bregman, J. N. 2005, ApJS, 157, 59
- Masters, K., 2005, PhD Thesis, Cornell University

- Mapelli, M., Colpi, M., & Zampieri, L. 2009, MNRAS, 395, L71
- Mapelli, M., Ripamonti, E., Zampieri, L., & Colpi, M. 2011, *Astronomische Nachrichten*, 332, 414
- Mapelli, M., Ripamonti, E., Zampieri, L., Colpi, M., & Bressan, A. 2010, MNRAS, 408, 234
- Miller, M. C., & Colbert, E. J. M. 2004, *International Journal of Modern Physics D*, 13, 1
- Mineo, S., Gilfanov, M., & Sunyaev, R. 2012, MNRAS, 419, 2095
- Moustakas, J., Kennicutt, R. C., Jr., Tremonti, C. A., Dale, D. A., Smith, J.-D. T., & Calzetti, D. 2010, ApJS, 190, 233
- Papaderos, P., Guseva, N. G., Izotov, Y. I., & Fricke, K. J. 2008, A&A, 491, 113
- Pilyugin, L. S., & Thuan, T. X. 2005, ApJ, 631, 231
- Prestwich, A. H., et al. 2007, ApJ, 669, L21
- Prestwich, A. H., et al. 2012, ApJ, 747, 150
- Ranalli, P., Comastri, A., & Setti, G. 2003, A&A, 399, 39
- Roberts, T. P., Kilgard, R. E., Warwick, R. S., Goad, M. R., & Ward, M. J. 2006, MNRAS, 371, 1877
- Roberts, T. P. 2007, Ap&SS, 311, 203
- Soria, R. 2007, IAU Symposium, 238, 235
- Soria, R., Cropper, M., Pakull, M., Mushotzky, R., & Wu, K. 2005, MNRAS, 356, 12
- Sutton, A. D., Roberts, T. P., Walton, D. J., Gladstone, J. C., & Scott, A. E. 2012, MNRAS, 423, 1154.
- Swartz, D. A., Ghosh, K. K., Tennant, A. F., & Wu, K. 2004, ApJS, 154, 519
- Swartz, D. A., Soria, R., & Tennant, A. F. 2008, ApJ, 684, 282
- Swartz, D. A., Soria, R., Tennant, A. F., & Yukita, M. 2011, ApJ, 741, 49
- Thuan, T. X., Bauer, F. E., Papaderos, P., & Izotov, Y. I. 2004, ApJ, 606, 213
- Walton, D. J., Roberts, T. P., Mateos, S., & Heard, V. 2011, MNRAS, 416, 1844

Zampieri, L., & Roberts, T. P. 2009, MNRAS, 400, 677

Zezas, A., Fabbiano, G., Baldi, A., Schweizer, F., King, A. R., Rots, A. H., & Ponman, T. J.
2007, ApJ, 661, 135

Table 8: 24 microns measurements and SFRs

Galaxy	Flux density (mJy)	Flux (10^{-13} erg/sec/cm ²)	L_{24} (10^{40} erg/sec)	SFR ($M_{\odot}yr^{-1}$)
HS 0822+3542	2.23±0.09	2.78±0.12	0.54±0.02	0.002±0.001
SBS 0940+544	1.60±0.10	2.01±0.13	1.47±0.09	0.005±0.003
KUG 1013+381	14.54±0.17	18.2±0.21	8.37±0.09	0.022±0.002
SBS 1415+437	16.67±0.15	20.8±0.19	2.70±0.02	0.008±0.001
UGCA 292	<0.87±0.31	1.09±0.34	0.08±0.03	0.0003±0.0010
HS 1442+4250	3.23±0.11	4.03±0.14	0.53±0.02	0.002±0.001
SBS 1102+606	1.33±0.10	1.67±0.11	0.79±0.06	0.003±0.002
I Zw 18	4.84±0.11	6.05±0.14	2.12±0.05	0.006±0.001
SBS 0335-052	67.25±0.20	84.10±0.25	278.94±0.84	0.480±0.013
SBS 0335-052W	0.14±0.04	0.018±0.005	0.58±0.17	0.002±0.005

NOTES: The SFR errors were calculated with error propagation. For the galaxy UGCA 292 we calculate the upper limits.

Table 9: Characteristics of the SINGS sample.

Galaxy	Morphology	Distance (Mpc)	$12+\log(\text{O}/\text{H})$	$L(\text{H}\alpha)_{\text{obs}}$ (10^{40} erg/sec)	SFR ($\text{M}_{\odot}/\text{yr}$)	N_{ULX}	N_{BKG}
High-metallicity galaxies							
NGC 0925	SAB(s)d	9.12	8.24-8.78	6.01	1.634	1	0.566
NGC 2403	SAB(s)cd	3.5	8.31-8.81	5.12	1.225	1	0.474
NGC 2841	SA(r)b	9.8	8.52-9.19	3.39	3.17	2	0.282
NGC 2976	SAc	3.5	8.30-8.98	0.87	0.334	0	0.028
NGC 3184	SAB(rs)cd	11.10	8.48-9.14	7.36	3.31	2	0.628
NGC 3198	SB(rs)c	13.68	8.32-8.87	6.85	3.71	1	0.493
NGC 3351	SB(r)b	10.1	8.60-9.22	3.71	3.907	0	0.093
NGC 3627	SAB(s)b	8.7	8.49-9.10	10.9	11.362	2	0.312
NGC 4559	SAB(rs)cd	11.1	8.25-8.79	10.6	2.545	3	0.578
NGC 4569	SAB(rs)ab	16.58	8.56-9.19	4.84	6.731	1	1.015
NGC 4625	SAB(rs)m	9.17	8.27-9.04	0.61	0.215	0	0.013
NGC 4736	(R)SA(r)ab	5.3	8.31-9.01	3.45	2.709	3	0.357
NGC 4826	(R)SA(rs)ab	5.6	8.59-9.2	4 4.05	2.732	0	0.209
NGC 5055	SA(rs)bc	7.82	8.42-9.13	7.71	6.172	2	0.613
NGC 5194	SA(s)bc	8.2	8.54-9.18	20.10	15.847	3	0.569
NGC 6946	SAB(rs)cd	5.0	8.40-9.04	16.5	16.437	1	0.4258
NGC 7331	SA(s)b	15.1	8.40-9.05	13.4	15.893	3	0.850
Intermediate-Metallicity Galaxies							
NGC 1705	SA0-	5.1	8.20-8.43	0.9	0.075	0	0.009
IC 2574	SAB(s)m	2.8	7.94-8.26	0.97	0.128	0	0.084
NGC 4236	SB(s)dm	4.45	8.07-8.56	1.3	0.183	0	0.411
IC 4710	SB(s)m	7.8	8.11-8.62	1.6	0.231	1	0.071
NGC 6822	IB(s)m	0.47	8.04-8.67	0.07	0.015	0	0.013
Low-Metallicity Galaxies							
Ho II	Im	3.5	7.68-8.07	0.64	0.073	1	0.087
DDO 053	Im	3.56	7.77-8.13	0.08	0.011	0	0.003
Ho IX	Im	3.3	7.61-7.98	0.01	0.009	1	0.008
NGC 5408	IB(s)m	4.8	7.81-8.23	1.16	0.023	1	0.004

NOTES: Galaxy morphologies are from the NASA/IPAC Extragalactic Database (NED). Adopted distances as derived by Masters (2005). Oxygen abundances are from Moustakas et al. (2010)

Table 10: Comparison of the SINGS and XMPGs sample.

	High	Intermediate	Low	XMPGs	Low+XMPG
$\sum N_{ULX}$	25	1	3	5	8
$\sum N_{BKG}$	7.5	0.6	0.1	1.3	1.4
$N_{ULX}(SFR)$	0.17 ± 0.042	0.65 ± 1.0	25.0 ± 14.6	4.5 ± 2.3	7.0 ± 2.7